PHYSICAL REVIEW B VOLUME 48, NUMBER 6 1 AUGUST 1993-II

Spectroscopic and tunable laser properties of Co^{2+}-doped single crystals

H. Manaa, Y. Guyot, and R. Moncorge
Laboratoire de Physico-Chimie des Matériaux Luminescents, Université de Lyon 1, 69622 Villeurbanne, France

(Received 18 September 1992; revised manuscript received 19 February 1993)

We present here a comparison of the general optical properties (absorptions, emissions, fluorescence decays) of various Co^{2+}-doped single crystals ($KZnF_3$, $KMgF_3$, MgF_2, and MgO) and the results of direct measurements of excited-state-absorption (ESA) cross sections and of laser experiments in Co^{2+}-doped $KZnF_3$ and MgF_2. The ESA measurements are made in the pump as well as in the emission domains. The data are interpreted, with some approximations, within the framework of the single-configurational-coordinate model and the Struck and Fonger formalism. The laser data (threshold, efficiency, and tunability) are obtained at room temperature and in the same pumping conditions (pulsed-type longitudinal pumping) for the two systems. It is shown that MgF_2:Co^{2+}, in spite of a stronger ESA at the usual pumping wavelength of 1.32 μm, leads to better laser performance than $KZnF_3$:Co^{2+} and that the fluorescence quantum efficiency of both systems is quite low.

I. INTRODUCTION

Many tunable solid-state laser systems have been studied and developed within the last decade. Indeed, many important applications, taking advantage of their broadband emissions, exist in the industrial, medical, and military domains as well as in fundamental research.

As with the recent and now very famous Ti:sapphire, we talk about single crystals doped with transition-metal ions of the iron group, Ti^{3+} ions, but also Cr^{4+}, Cr^{3+}, V^{2+}, Ni^{2+}, and Co^{2+}. With the color center laser crystals (crystals in which luminescent defects have been created intentionally) the transition-metal ion (TMI) laser crystals lead to optical bands between electronic and vibrational states called vibronic sidebands. Their laser gains are generally much weaker than those of the color center lasers but their optical properties are more stable and much more power can be extracted. In addition, most of the color center lasers require cryogenic cooling.

The vibronic laser systems based on Co^{2+}-doped materials are unique because, in principle, they allow tunabilities over about 1000 nm in a wavelength domain extending from about 1500 to 2500 nm. They are the only TMI lasers which emit a tunable radiation beyond 2000 nm and they are among the first systems based on transition-metal ions to have led to tunable laser action at the beginning of the sixties;[1-3] at that time the crystal was pumped by flash lamps and was maintained at liquid-nitrogen (LN) temperature. These systems were neglected for a while and then emerged again at the end of the seventies and at the beginning of the eighties. It was the first demonstration of the CW (continous wave) tunable laser effect under laser pumping at LN temperature, in MgF_2:Ni^{2+} yttrium-aluminum garnet [YAG:Nd laser excitation at 1.32 μm (Ref. 4) or krypton laser excitation at 755 nm (Refs. 5 and 6)], in MgF_2:Co^{2+} [YAG:Nd laser excitation at 1.32 μm (Refs. 7 and 8)] and in $KZnF_3$:Co^{2+} [argon laser excitation at 514.5 nm (Refs. 9 and 10)]. At the same time, many Cr^{3+}-doped laser materials, such as alexandrite ($BeAl_2O_4$:Cr^{3+}) appeared and were found to work at room temperature, under a flash lamp as well as laser pumping,[11,12] but essentially in a restricted wavelength domain between 700 and 900 nm. It is only recently that high-temperature laser operation of the Co^{2+}-doped laser materials, essentially MgF_2:Co^{2+}, has been reported.[13,14]

II. MATERIALS

$KZnF_3$ and $KMgF_3$ are both fluoroperovskites of type AMF_3 where M is a divalent metal ion surrounded by six nearest-neighbor fluors. In the doped compounds, the Co^{2+} ions substitute for M and occupy octahedral symmetry sites.[15,16] The metal-fluor distance in $KZnF_3$ with a value of about 2.026 Å is slightly larger than in $KMgF_3$ where it is about 2.00 Å; thus the local crystal field experienced by the Co^{2+} ion in $KZnF_3$ is expected to be smaller than in $KMgF_3$.

Two crystals of $KZnF_3$:Co^{2+}, grown by the Czokralski method by M. Gesland of the University of Le Mans in France, were used in the present study. They are good single crystals of laser quality and they both contain 1.5×10^{20} Co^{2+} ions/cm^3 (or 1.7% Co^{2+}/Mg^{2+}). One was used for the spectroscopy and the other was cut and polished for the laser measurements.

Only one crystal of $KMgF_3$:Co^{2+}, provided by Professor D. Simkin of McGill University in Canada, was available. It contained 1.52×10^{20} Co^{2+} ions/cm^3 (or 1% Co^{2+}/Mg^{2+}) and its small size (a few mm^3) and poor optical quality only allowed spectroscopic measurements.

MgF_2 belongs to the rutile family. The unit cell is tetragonal and the Mg^{2+} ion is surrounded by six fluorines occupying the tops of a distorted octahedra of D_{2h} site symmetry.[17] The nearest neighbor Mg-F distances are of the order of 1.98 Å, thus shorter than in the above perovskites. This makes the lattice stiffer and the local crystal field about the Co^{2+} dopant probably stronger.

Three crystals were available. The one with the best

0163-1829/93/48(6)/3633(13)/$06.00

optical quality contains 3.73×10^{20} Co^{2+} ions/cm^3 (or 1% Co^{2+}/Mg^{2+}) and was cut and polished for the laser measurements; it was grown by the Czokralski technique at the LETI/CEA in Grenoble, France and provided to us by Dr. J. J. Aubert. The other crystals, grown by the Bridgman method, were used for the spectroscopy. The one, provided to us by Professor Margerie of the University of Caen in France, contained 4.44×10^{20} Co^{2+} ions/cm^3 (1.4% Co^{2+}/Mg^{2+}) and the other, provided by Professor McClure of Princeton University (USA), contained 1.55×10^{20} Co^{2+} ions/cm^3 (or 0.5% Co^{2+}/Mg^{2+}).

MgO is a face-centered-cubic system in which the Mg^{2+} ions are surrounded by six oxygens at about 2.1 Å. The crystal used in our spectroscopic study was provided to us by Dr. Abraham from the Oak Ridge National Laboratory (USA); it contained 2.3×10^{20} Co^{2+} ions/cm^3.

The three fluorides $KZnF_3$, $KMgF_3$, and MgF_2 have low fusion temperatures, 870°, 1070°, and 1261 °C respectively, compared to that of MgO with 2852 °C. This makes their crystal growth much easier but they are more fragile; polishing is difficult and their growth in the form of large laser rods is delicate. We note that the fusion temperature of the fluorides increases as the metal-fluor distance decreases. This increasing lattice stiffness likely has consequences on the refractive index of the materials since it takes values of 1.48, 1.4, and 1.38 in $KZnF_3$, $KMgF_3$, and MgF_2, respectively, but also on their thermal conductivity with room-temperature values of 6 and 11.6 W/m/K in $KZnF_3$ and MgF_2, respectively.

Consequently, because of its better thermomechanical properties, MgF_2 already appears as a better laser material. We shall see in this study that it is confirmed by its optical properties and its laser performance when it is doped by Co^{2+} ions.

III. SPECTROSCOPY AND FLUORESCENCE DYNAMICS

Each of the compounds $KZnF_3$, $KMgF_3$, MgF_2, and MgO, doped either by Ni^{2+} or Co^{2+} ions, was already studied in the past, more or less thoroughly, for its optical and laser properties.[1–10,13–33] Thus the available data are very numerous and we could have used some of them directly if we had not noticed a number of puzzling observations, experimental uncertainties, or misinterpretations. In addition, only the low-energy infrared optical transitions were really studied in some detail. As we were interested in the vibronic absorption and emission transitions with the ground state of the active ions as well as in the vibronic transitions between their excited states, we needed a very complete description of all the energy levels, from the infrared to the near ultraviolet, and we needed to know all the phonon energies which are involved in the radiative and nonradiative processes in each compound, which could not be obtained without analyzing the optical properties of these compounds with a common systematic procedure. This is the purpose of this section.

The assignment of the various features (lines and bands) observed in the absorption spectra and the determination of the positions and the description of the profiles of the main bands in the linear electron-phonon coupling approximation (the same interacting phonons of energy $\hbar\omega_0$ in all the energy levels) have allowed us first to confront the results with the predictions of the single-configuration-coordinate (SCC) model, with the help of the Struck and Fonger (SF) formalism.[34] From that we have deduced the Huang-Rhys[35] electron-phonon coupling factor S_e associated with each excited state (this parameter determines the relative positions of the excited-state and ground-state potential curves in the SCC diagrams) and the effective phonon energy $\hbar\omega_0$, as we already have done in the past in the case of the Ni^{2+}- and V^{2+}-doped systems.[33,36] This first approach has led to a better positioning of all the zero-phonon energy levels and to the values of the Racah (B and C), crystal-field (Dq) and spin-orbit (ξ) parameters which give, by diagonalizing the well-known Tanabe-Sugano matrices, the best description of these levels.

Then the analysis of the thermal evolution of the widths (or first moments) and of the intensities (oscillator strengths) of the visible and infrared-absorption bands has allowed us to determine the phonon energies $\hbar\omega_1$ and $\hbar\omega_2$, and the analysis of the vibronic structures, which characterize these bands at low temperature, the phonon energies $\hbar\omega_3, \hbar\omega_4, \ldots,$ values which can be related, in principle, with the phonon density of states in each material.[17–20]

The evaluation of the phonon energies $\hbar\omega_1$ and $\hbar\omega_2$ assumed that the bands are associated with vibronic transitions (forced) electric dipole allowed by odd-parity phonons, in which case the widths δ and the intensities I of the bands should vary according to the well-known equation[37]

$$S(T)=S(T=0)\coth(\hbar\omega/2kT)\ , \tag{1}$$

with

$$S=\delta \text{ or } I \text{ and } \hbar\omega_1=\hbar\omega_2=\hbar\omega\ .$$

We shall see that some bands have a strong magnetic dipole character, in which case the above equation does not apply correctly and leads to very different values of $\hbar\omega_1$ and $\hbar\omega_2$.

The analysis of the lines observed in the low-temperature infrared emission spectra has led to the phonon energies $\hbar\omega_5$ and $\hbar\omega_6$. The position and the shape of the underlying vibronic sidebands then have been confronted, as in absorption, with the predictions of the SCC model by using the same effective phonon energy $\hbar\omega_0$ as above.

Finally, the thermal variation of the infrared fluorescence lifetimes has been studied and described within the framework of the same SCC model and new Huang-Rhys factors S_{NR} and phonon energies $\hbar\omega_{NR}$ have been derived. We remember that the fluorescence lifetime τ_F, in the case of nonradiative transitions, is related to the radiative lifetime τ_R of the emitting level and to the nonradiative probability W_{NR} by the expression

$$\tau_F^{-1}=\tau_R^{-1}+W_{NR}\ , \tag{2}$$

and that W_{NR} is related to S_{NR} and $\hbar\omega_{NR}$ by

$$W_{\mathrm{NR}} = N_{\mathrm{uv}} \times W_p(S_{\mathrm{NR}}, \hbar\omega_{\mathrm{NR}}, T) , \tag{3}$$

where p stands for the mean number of phonons of energy $\hbar\omega_{\mathrm{NR}}$ needed to overcome the excited-state–ground-state energy mismatch of energy $\Delta E = p\hbar\omega_{\mathrm{NR}}$, N_{uv} is a coupling constant and W_p the line-shape functions or Franck-Condon weighting factors defined in the SF theory.

The value of the radiative lifetime τ_R is generally deduced from the absorption coefficient k of the emitting level, level ${}^4T_2$ in the case of Co^{2+}, according to the expression[38]

$$\tau_R^{-1} = 8\pi n^2 \bar{\nu}^2 \frac{g_1}{g_2} \frac{c}{N} \int k(\bar{\nu}) d\bar{\nu} , \tag{4}$$

where g_1/g_2 is the ratio of the excited- to ground-state ${}^4T_2 \rightarrow {}^4T_{1a}$ degeneracy (here equal to 1), N is the active ion concentration, and $\bar{\nu}$ is the wave number in cm^{-1}. In the case of π and σ polarized spectra (the case of $\mathrm{MgF_2{:}Co^{2+}}$) k is given by $(k^{\pi} + 2k^{\sigma})/3$ where k^{α} stands for the absorption coefficient in the α polarization.

Sometimes the integration is made over the entire absorption band. However, in the case of a large spin-orbit and/or a large crystal-field splitting in the excited state, not all the components contribute to the emission and the radiative lifetime can be underestimated. As was done by Sturge[18] in the case of $\mathrm{KMgF_3{:}Co^{2+}}$, it is more correct to first make the integration over the zero-phonon line and to derive the corresponding emission rate W_{NP} by using Eq. (4), then to calculate the ratio of the total emission intensity (measured in photon units) to that of this zero-phonon line to get the total emission rate $W_R = \tau_R^{-1}$, which can be done only when low-temperature spectra are available.

From Eq. (4) we also note that the radiative lifetime might decrease as a result of an increase in transition strength due to dynamical coupling via odd-parity phonons. In this case τ_R^{-1} takes a form analogous to (1), i.e.,

$$\tau_R^{-1} = \tau_R^{-1}(T=0) \coth(\hbar\omega/2kT) . \tag{5}$$

A. Spectral data

The absorption and the infrared emission spectra of $\mathrm{MgF_2{:}Co^{2+}}$ and $\mathrm{KZnF_3{:}Co^{2+}}$ recorded at low and high temperatures are reported in Figs. 1–4.

The broadbands observed in absorption are assigned to the three spin-allowed transitions characteristic of the Co^{2+} ion [Ar($3d^7$) electron configuration] in an octahedral environment, ${}^4T_{1a} \rightarrow {}^4T_2$ around 7000 cm^{-1} ${}^4T_{1a} \rightarrow {}^4A_2$ around 15 000 cm^{-1}, and ${}^4T_{1a} \rightarrow {}^4T_{1b}$ around 20 000 cm^{-1}. The emission bands are assigned to the reverse transitions ${}^4T_2 \rightarrow {}^4T_{1a}$. The widths of these bands are simply explained using the strong-field approach in which it is admitted that the degeneracy of the $3d$ orbitals is lifted and are split into two e_g and three t_{2g} components. Indeed these bands involve transitions between a ground state ${}^4T_{1a}$ and excited states ${}^4T_2$, ${}^4A_2$, and ${}^4T_{1b}$, having different electron configurations $t_2^5 e_g^2$, $t_2^4 e_g^3$, $t_2^3 e_g^4$, and $t_2^4 e_g^3$, respectively; thus different equilibrium configurations. We also understand in this approach why the ${}^4T_{1a} \rightarrow {}^4A_2$ optical band is so weak; because it involves a two-electron jump.

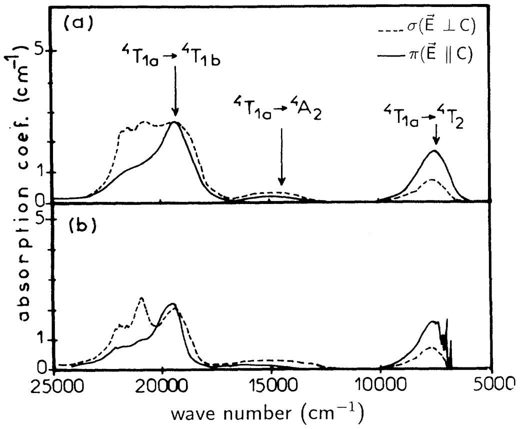

FIG. 1. Polarized absorption spectra of $\mathrm{MgF_2{:}0.5\%\ Co^{2+}}$ (thickness = 1.62 mm) at (a) $T = 300$ K and (b) 15 K.

In $\mathrm{KMgF_3{:}Co^{2+}}$ as well as in $\mathrm{KZnF_3{:}Co^{2+}}$ and $\mathrm{MgF_2{:}Co^{2+}}$ the high-energy band is flanked at around 22 000 cm^{-1} by another band which is associated to a ${}^4T_{1a} \rightarrow {}^2T_{1b}$ spin-forbidden transition, partially allowed through spin-orbit coupling between states ${}^2T_{1b}$ and ${}^4T_{1b}$. It is also likely that the band around 15 000 cm^{-1} is not due solely to the ${}^4T_{1a} \rightarrow {}^4A_2$ transition mentioned above; based on the calculations made hereafter it must be flanked on its low-energy side by a ${}^4T_{1a} \rightarrow {}^2E$ transition.

The sharp features observed at low temperature are zero-phonon lines and/or phonon satellites. As an illustration, we show in Fig. 5 the low-temperature infrared-absorption and emission spectra (in cm^{-1} instead of nm) of $\mathrm{KZnF_3{:}Co^{2+}}$ from which the phonon energies $\hbar\omega_3$, $\hbar\omega_4$, $\hbar\omega_5$, and $\hbar\omega_6$ are deduced.

At this point it is worth noting that no fluorescence at all could have been detected in $\mathrm{MgO{:}Co^{2+}}$, even at very low temperature ($T = 10$ K), though this fluorescence was reported in the past.[25] This is one of the puzzling questions that we mentioned at the beginning that we were unable to solve.

Finally, from all these data we have been able to obtain all the energies of the phonons which participate in the radiative vibronic processes. These energies are gathered in Table I.

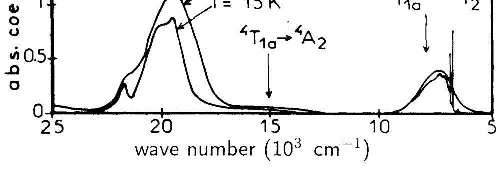

FIG. 2. Absorption spectra of $\mathrm{KZnF_3{:}1.7\%\ Co^{2+}}$ (thickness = 1.48 mm) at $T = 15$ and 300 K.

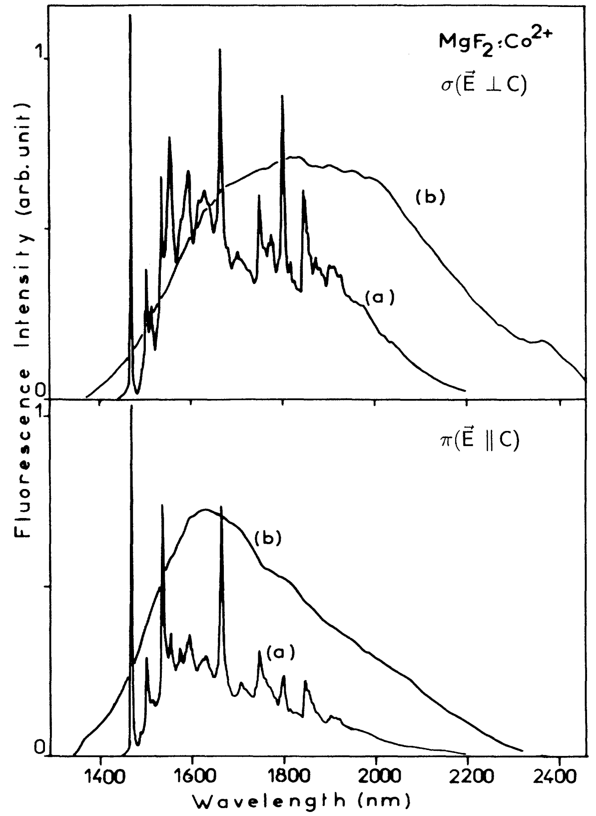

FIG. 3. Polarized emission spectra of MgF$_2$:0.5% Co^{2+} at (a) $T=12$ K and (b) 300 K.

The energies of the "enabling" phonons determined from the thermal evolution of the widths ($\hbar\omega_{1a}$) and of the intensities ($\hbar\omega_{2a}$) of the infrared-absorption bands associated with the $^4T_{1a}\rightarrow{}^4T_2$ optical transition are very different from each other, except in the case of MgO:Co^{2+}. On the contrary, those determined from the widths ($\hbar\omega_{1b}$) and the intensities ($\hbar\omega_{2b}$) of the visible absorption band associated with the $^4T_{1a}\rightarrow{}^4T_{1b}$ transition are very close in all the systems. This discrepancy means that the above law in coth applies better in the case of the high-energy (visible) than in the low-energy (infrared) absorption band; it is a consequence of the predominant character of each band, of electric dipole and magnetic dipole character, respectively.

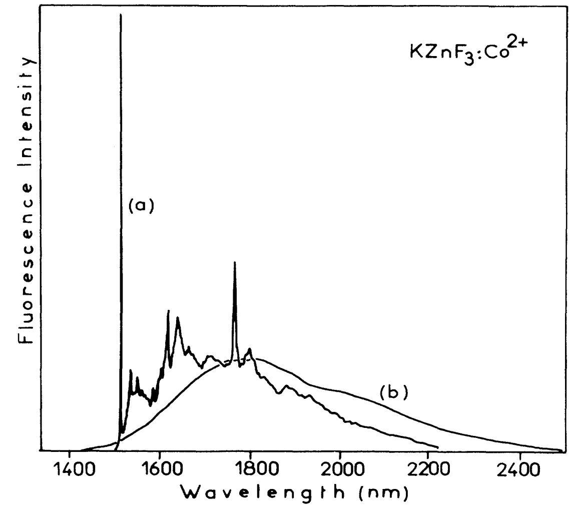

FIG. 4. Emission spectra of KZnF$_3$:1.7% Co^{2+} at (a) $T=12$ K and (b) 300 K.

Nevertheless, whatever the intensity enabling process, the intensity of the infrared-absorption band increases between low and room temperature, by about a factor of 1.17 in the case of KZnF$_3$, KMgF$_3$, and MgF$_2$ and by about a factor of 1.9 in the case of MgO. As we shall see in the following, these variations will be neglected in the derivation [from Eq. (2)] of the nonradiative rate W_{NR} because $W_{\mathrm{NR}} \gg \tau_R^{-1}$ but they will be taken into account explicitly in the derivation of the stimulated emission cross sections.

The spectral profiles of the absorption and emission bands are described very satisfactorily by taking $\hbar\omega_0$ equal to the weighted average energy of the phonon density of states in each material[17–20] and we believe that it is justified by the number of phonons of different energies which precisely come into play in each system. This seems a quasigeneral result in the case of the transition-metal ions of the iron group such as Co^{2+}. This is not the case with the rare-earth ions for which the electron-phonon coupling is much weaker and the most important phonon modes are generally the high-energy totally symmetric phonon modes A_{1g}. As an illustration we show in Fig. 6 the fitting of the band shape $F(\bar{\nu})=N(\bar{\nu})/\bar{\nu}^3$ of the

TABLE I. Comparison of the different phonon energies (in cm^{-1}) derived from the absorption and emission data (half widths δ and integrated intensities I with temperature T, vibronic structures at low temperature), with the mean phonon energy $\hbar\omega_0$ in each material.

	Abs. $^4T_2$		Abs. $^4T_{1b}$		Abs. $^4T_2$		Em. $^4T_2$		Mean
	δ(T)	I(T)	δ(T)	I(T)	vibr.	str.	vibr.	str.	energy
	$\hbar\omega_{1a}$	$\hbar\omega_{2a}$	$\hbar\omega_{1b}$	$\hbar\omega_{2b}$	$\hbar\omega_{3a}$	$\hbar\omega_{4a}$	$\hbar\omega_5$	$\hbar\omega_6$	$\hbar\omega_0$
KZnF$_3$:Co^{2+}	330	530	232	280	161	370	90	110	223
KMgF$_3$:Co^{2+}	260	490	225	275	197	· · ·	· · ·	· · ·	285
MgF$_2$:Co^{2+}	390	510	250	250	200	410	85	293	326
MgOCo^{2+}	270	260	295	295	170	405	· · ·	· · ·	405

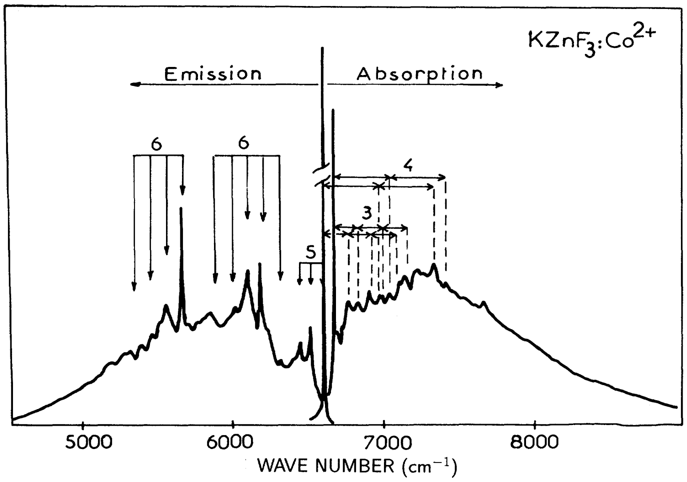

FIG. 5. Infrared absorption and emission spectra of KZnF$_3$:Co^{2+} at low temperature ($T \cong 12$ k) showing the phonon spacings $\hbar\omega_3$ (3), $\hbar\omega_4$ (4), $\hbar\omega_5$ (5), and $\hbar\omega_6$ (6).

infrared emission in KZnF$_3$:Co^{2+} at low and high temperatures with the sum of three line-shape functions $W_p(S,\hbar\omega_0,T)$ (the same kind of function is used to describe the radiative and nonradiative processes). These functions are associated at low temperature with the three zero-phonon lines located at 6595, 6302 (6595−293), and 5655 (6595−940) cm^{-1} (see Table III) and corresponding to the same parameters S_e and $\hbar\omega_0$ used in absorption, i.e., $S=2.6$ and $\hbar\omega_0=223$ cm^{-1}. At room temperature the zero-phonon origins were fixed at 6395, 6102, and 5455 cm^{-1} to account for the effect of the thermal expansion of the lattice. Indeed, when the temperature of the crystal is increased, the lattice slightly expands; thus the Co^{2+} active ion experiences a lower crystal field and the optical transition energies, (this can be seen easily on the Tanabe-Sugano diagram of the Co^{2+} ion) are reduced. Assuming that the shift of the zero-phonon levels roughly follows that of the phonon sidebands and accounting for the thermal population of each state, we find that the $^4T_{1a}$-$^4T_2$ transition energy should be reduced by (250±50) cm^{-1} in the case of KMgF$_3$:Co^{2+}, in good agreement with previous works,[27] and by (200±50) and (150±50) cm^{-1} in the case of KZnF$_3$:Co^{2+} and MgF$_2$:Co^{2+}, respectively.

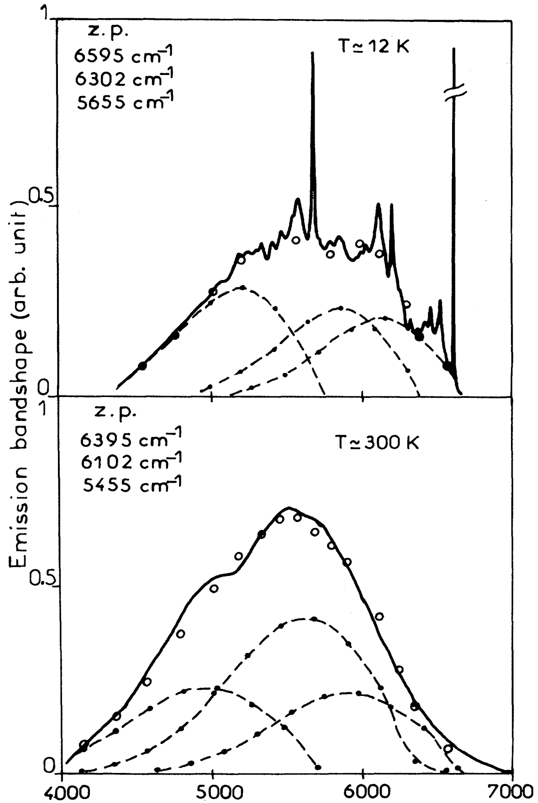

FIG. 6. Fitting of the infrared emission band shape $F(\bar{\nu})$ (——) in KZnF$_3$:Co^{2+}, at low and high temperatures, with the sum (○) of three SF line-shape functions W_p (●) and with the same parameters $S \cong 2.6$ and $\hbar\omega_0 \simeq 223$ cm^{-1} but different zero-phonon (zp) positions.

B. Lifetime data

The lifetime data are reported in Fig. 7. The fits of Eq. (3) to the data are reported in Fig. 8. The $^4T_{1a}$-$^4T_2$ energy mismatch introduced in the calculations as the product $p\hbar\omega_{\mathrm{NR}}$ is taken as the energy gap between the mean positions of the spin-orbit components in the excited and the ground states. The radiative lifetime is that deduced from the low-temperature absorption and emission spectra and its slight variation (see Sec. III A) between low and high temperatures was neglected. The fitting parameters are gathered in Table II.

We first note that the nonradiative probability in these Co^{2+}-doped materials is very strong. It is the reason why the thermal variations of the radiative lifetimes were neglected in the previous fits. This strong nonradiative probability can be explained by using group-theory arguments. Indeed the probability W_{NR} depends on transition matrix elements of the form $\langle \Gamma_a / \Gamma_p / \Gamma_b \rangle$ where Γ_a and Γ_b are the irreducible representations characterizing the ground and the excited states, respectively, and Γ_p is the interacting phonon mode. In the case of Ni^{2+}, Cr^{3+}, and V^{2+} in low-field systems, the lower-energy optical

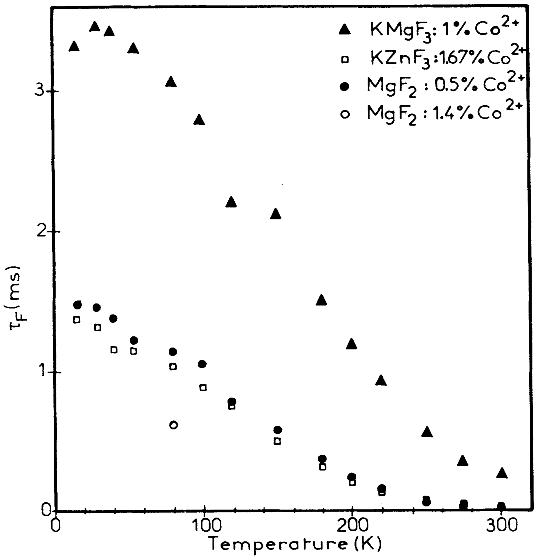

FIG. 7. Temperature variations of the fluorescence lifetimes in various Co^{2+}-doped compounds.

transitions occur between orbital states A_2 and T_2; in the case of Co^{2+} they occur between states T_1 and T_2. Group theory thus indicates that only T_{1g}-promoting modes can be efficient in the case of Ni^{2+}, Cr^{3+}, and V^{2+} ions, while A_{2g}, E_g, T_{1g}, and T_{2g} modes can act in the case of Co^{2+}. Knowing that the coupling to T_{1g} modes, which corresponds to a simple rotation of the immediate ligands, is usually very weak, we can conclude, in good agreement with the experimental observations, that the nonradiative processes are much more efficient in the case of Co^{2+} than in the case of the other ions.

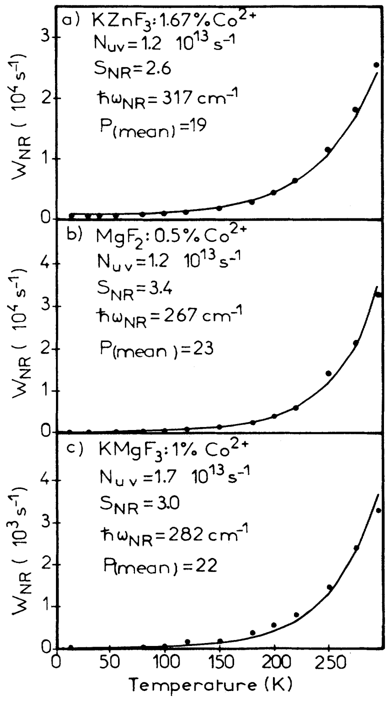

FIG. 8. Nonradiative emission rate W_{NR} (●) and fits with Eq. (3) (——) in Co^{2+}-doped $KZnF_3$, $KMgF_3$, and MgF_2.

TABLE II. Fitting parameters to the lifetime data and values of the radiative lifetimes derived from the absorption data in each material.

	N_{uv} (s^{-1})	S_{NR}	$\hbar\omega_{NR}$ (cm^{-1})	p (mean)	τ_R (ms) $T=12$ K
$KZnF_3:Co^{2+}$	1.21×10^{13}	2.6	317	19	3.2
$MgF_2:Co^{2+}$	1.17×10^{13}	3.4	267	23	6
$KMgF_3:Co^{2+}$	1.71×10^{13}	3.0	282	22	4.4

From Table I we also note that the energies $\hbar\omega_{NR}$ of the phonons involved in the nonradiative transitions can be very difficult from the mean energies $\hbar\omega_0$ involved in the radiative mechanisms. It means that the "accepting" phonons in the radiative and the nonradiative processes are not necessarily the same, which makes sense.

In the end we shall mention that the radiative lifetimes calculated from the entire absorption band or from the zero-phonon line and the emission spectrum registered at low temperature only differ significantly in the case of $MgF_2:Co^{2+}$. In this system the lifetimes differ by about a factor of 4, with 1.6 ms from the entire absorption band against 6 ms via the zero-phonon line, which is very important and will be essential in the interpretation of our laser data.

C. Energy levels

To illustrate our purpose, Fig. 9 shows the energy-level diagram which is obtained in the case of $KZnF_2:Co^{2+}$ from the position of each of the experimentally observed (or estimated) and calculated zero-phonon levels (func-

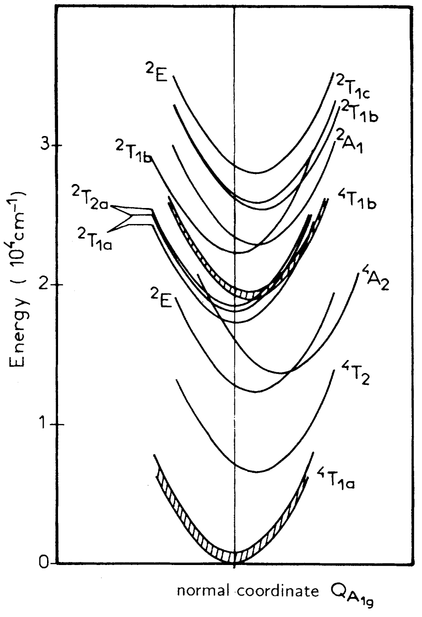

FIG. 9. Energy-level diagram (SCC model) of $KZnF_3:Co^{2+}$.

tion of the Dq, B, C, and ξ parameters) and from the shift of each of the associated potential curves (function of the product $S\hbar\omega_0$).

The results for the four compounds are given in Tables III–VI. The best agreements between the experimentally observed (or estimated) and calculated energy levels are found in the case of the cubic compounds MgO, $KZnF_3$, and $KMgF_3$ because all the contributions to the Hamiltonian of the systems could have been included. The agreement is not so good in the case of the orthorhombic system MgF_2 because it was assumed, for simplicity, that the overall splitting of the levels caused by the tetragonal distortion added to the spin-orbit coupling could be approximated by an effective (fictive) spin-orbit coupling of constant ξ_{eff}. The number of sublevels is not complete but the approximative position and the extent of each excited state is correct and will be precise enough to allow us to predict in Sec. IV, the energies of the excited-state absorption (ESA) transitions.

TABLE III. Observed (or estimated) and calculated energy levels (with $Dq = 705\ \mathrm{cm}^{-1}$, $B = 900\ \mathrm{cm}^{-1}$, $C = 4100\ \mathrm{cm}^{-1}$, and $\xi = 535\ \mathrm{cm}^{-1}$) along with energy shifts of potential curves in $KZnF_3{:}Co^{2+}$ (in cm^{-1}).

Energy levels		Calculated energies	Observed (or estimated) energies	$S_e\hbar\omega_0$
$^4T_{1a}$	Γ_6	0	0	
	Γ_{8a}	355	293	
	Γ_{8b}	936	940	
	Γ_7	1043	. . .	
$^4T_2$	Γ_6	6624	6595	575
	Γ_{8a}	6679	6603	
	Γ_{8b}	6773	6675	
	Γ_7	6976	. . .	
^2E	Γ_8	12 436		605
$^4A_2$	Γ_8	13 832		2535
$^2T_{2a}$	Γ_8	17 450		2
	Γ_6	18 046		
$^2T_{2a}$	Γ_8	18 124		4
	Γ_7	18 333		
$^4T_{1b}$	Γ_{8a}	19 027	(18 700)	464
	Γ_7	19 043		
	Γ_{8b}	19 181		
	Γ_6	19 600	(19 750)	
$^2T_{1b}$	Γ_6,Γ_8	22 220	(21 350)	8
$^2A_1$	Γ_6	23 104		575
$^2T_{2b}$	Γ_8,Γ_7	25 555		880
$^2T_{1c}$	Γ_8,Γ_6	26 120		332
^2E	Γ_8	28 087		635

TABLE IV. Observed (or estimated) and calculated energy levels (with $Dq = 740\ \mathrm{cm}^{-1}$, $B = 920\ \mathrm{cm}^{-1}$, $C = 4140\ \mathrm{cm}^{-1}$, and $\xi = 520\ \mathrm{cm}^{-1}$) along with energy shifts of potential curves in $KMgF_3{:}Co^{2+}$ (in cm^{-1}).

Energy levels		Calculated energies	Observed (or estimated) energies	$S_e\hbar\omega_0$
$^4T_{1a}$	Γ_6	0		
	Γ_{8a}	346		
	Γ_{8b}	914		
	Γ_7	1012	. . .	
$^4T_2$	Γ_6	6915	6914	600
	Γ_{8a}	6965	6924	
	Γ_{8b}	7062	6982	
	Γ_7	7257	. . .	
^2E	Γ_8	12 335		630
$^4A_2$	Γ_8	14 465		2670
$^2T_{1a}$	Γ_8	17 670		2
	Γ_6	18 238		
$^2T_{2a}$	Γ_8	18 334		4
	Γ_7	18 549		
$^4T_{1b}$	Γ_{8a}	19 582	(19 200)	485
	Γ_7	19 589		
	Γ_{8b}	19 723		
	Γ_6	20 139	(19 860)	
$^2T_{1b}$	Γ_6,Γ_8	22 620	(21 500)	8
$^2A_1$	Γ_6	23 502		610
$^2T_{2c}$	Γ_8,Γ_7	25 900		940
$^2T_{1c}$	Γ_6,Γ_8	26 690		575
^2E	Γ_8	28 688		677

IV. EXCITED-STATE ABSORPTION

Because it can be very detrimental for laser action, excited-state absorption in the pump as well as in the emission domain of the TMI laser systems, is a very important phenomenon and must be studied very carefully.

TABLE V. Observed (or etimated) and calculated energy levels (with $Dq = 730\ \mathrm{cm}^{-1}$, $B = 920\ \mathrm{cm}^{-1}$, $C = 4140\ \mathrm{cm}^{-1}$, and $\xi_{\mathrm{eff}} = 520\ \mathrm{cm}^{-1}$) along with energy shifts of potential curves in $MgF_2{:}Co^{2+}$ (in cm^{-1}).

Energy levels		Calculated energies	Observed (or estimated) energies	$S_e\hbar\omega_0$
$^4T_{1a}$	Γ_6	0	0	
	Γ_{8a}	346	110	
			798	
	Γ_{8b}	914	1091	
	Γ_7	1012	1256	
			1398	
$^4T_2$	Γ_6	6826	6801	645
			6810	
	Γ_{8a}	6876	6880	
	Γ_{8b}	6972	6893	
	Γ_7	7168	6923	
^2E_a	Γ_8	12 427		680
$^4A_2$	Γ_8	14 276		2850
$^2T_{1a}$	Γ_8	17 669		0
	Γ_6	18 241		
$^2T_{2a}$	Γ_8	18 330		3
	Γ_7	18 544		
$^4T_{1b}$	Γ_{8a}	19 501	(19 000)	519
	Γ_7	19 509		
	Γ_{8b}	19 647	(20 500)	
	Γ_6	20 060		
$^2T_{1b}$	Γ_6,Γ_8	22 580	(22 000)	10
$^2A_1$	Γ_6	23 445		653
$^2T_{2b}$	Γ_7,Γ_8	25 656		369
$^2T_{1c}$	Γ_6,Γ_8	26 602		614
^2E_b	Γ_8	28 593		723

TABLE VI. Observed (or estimated) and calculated energy levels (with $Dq = 880$ cm^{-1}, $B = 780$ cm^{-1}, $C = 3510$ cm^{-1}, and $\xi = 475$ cm^{-1}) along with energy shifts of potential curves in MgO:Co^{2+} (in cm^{-1}).

Energy levels		Calculated energies	Observed (or estimated) energies	$S_e \hbar\omega_0$
$^4T_{1a}$	Γ_6	0	0	
	Γ_{8a}	313	330	
	Γ_{8b}	815	890	
	Γ_7	903	930	
^2E_a	Γ_8	8089	8049	527
$^4T_2$	Γ_6	8198	8141	500
	Γ_{8a}	8244	8168	
	Γ_{8b}	8338	8208	
	Γ_7	8507		
$^4A_2$	Γ_8	17 138		2210
$^2T_{1a}$	Γ_8	14 969		0
	Γ_6	15 426		
$^2T_{2a}$	Γ_8	15 636	17 125	3
	Γ_7	15 844		
$^4T_{1b}$	Γ_{8a}	18 440	(18 750)	430
	Γ_7	18 737		
	Γ_{8b}	18 742		
	Γ_6	19 000	(19 500)	
$^2T_{1b}$	Γ_6	19 947	(20 600)	8
$^2A_1$	Γ_6	22 046		506
$^2T_{2b}$	Γ_7	23 646		286
$^2T_{2c}$	Γ_8	23 865		780
$^2T_{1c}$	Γ_6	24 999		476
^2E_b	Γ_8	26 743		560

The ESA cross section spectra of MgF$_2$:Co^{2+} and KZnF$_3$:Co^{2+} were recorded both at cryogenic ($T \cong 80$ K) and at room temperature by using a standard pump-probe experimental arrangement that we have already described in another paper.[36] Very briefly, in this experiment, the transmission of a weak CW probe beam (that of a tungsten halogen lamp dispersed by a monochromator) is compared in the presence and in the absence of a pump pulse (that of a pulsed laser). The resulting absorption difference (AD) signal is a transient signal, the relaxation dynamics of which is related to that of the absorbing state. When the pulsed laser only excites a few percent of the active ions and when ESA occurs in the metastable emitting state, the AD signal decays with about the same time constant as the fluorescence intensity. This allows us to ascertain the nature of the absorbing excited state.

In the case of MgF$_2$:Co^{2+} and KZnF$_3$:co^{2+}, we used the pulsed radiation of a frequency-doubled Nd:YAG laser at 532 nm to excite the Co^{2+} ions in their $^4T_{1b}$ excited state. The AD signals were all characteristic of absorptions in the emitting state $^4T_2$ after rapid multiphonon relaxation (less than a few ns, the width of the pump pulse). The spectra were registered from 350 to 1450 nm.

Between about 350 to 700 nm, the AD spectra exactly mimic the ground-state absorption (GSA) spectra which indicate negligible ESA cross sections in this wavelength domain.

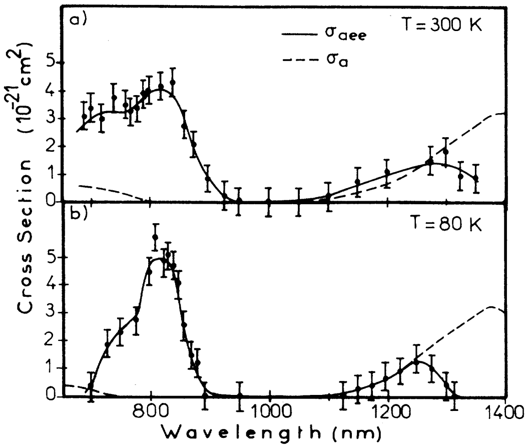

FIG. 10. GSA (— — —) and ESA (——) cross section spectra in KZnF$_3$:Co^{2+} at (a) $T = 300$ K and (b) 80 K between 700 and 1450 nm.

On the contrary, as shown in Figs. 10 and 11, beyond 700 nm, two broad ESA bands clearly appear around 800 and 1250–1300 nm and these bands have peak cross sections σ_{esa} of the same order of magnitude (around 2×10^{-21} cm^2) as those of the GSA bands labeled σ_a.

We note that strong ESA occurs in MgF$_2$:Co^{2+} at around 1320 nm, the usual pumping wavelength of this laser crystal, and that it is stronger than in KZnF$_3$:Co^{2+}. We also note that ESA is negligible in the emission domain beyond 1400 nm in KZnF$_3$ and beyond about 1450 nm in MgF$_2$; which is a good point for laser operation in these materials.

The positions and the shapes of the ESA bands can be confronted now with the predictions of the SCC model. Use is made of that by the data reported in Tables II and V and the SF theory, by considering the relative positions in the SCC diagrams of the potential curves associated with each excited level of higher energy to that of the

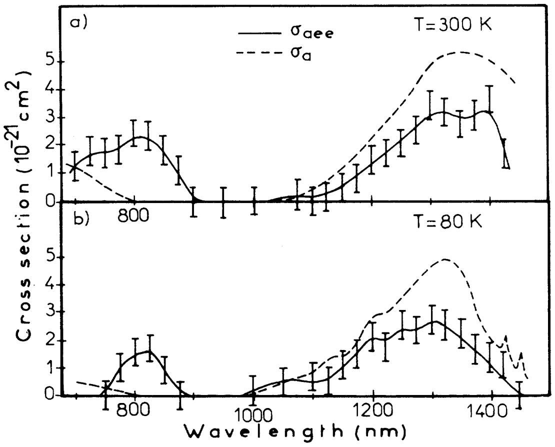

FIG. 11. σ polarized ($E \perp c$) GSA (— — —) and ESA (——) cross section spectra in MgF$_2$:Co^{2+} at (a) $T = 300$ K and (b) 80 K between 700 and 1450 nm.

emitting level $^4T_2$, and the potential curve associated with this new reference level is now determined by the parameters $S_{\rm int}$ and $\hbar\omega_0$. Tables VII and VIII give these new values along with the assignments and the energies (calculated from the lowest SO component of state $^4T_2$ in each compound) of the corresponding ESA transitions.

Because of the spin selection rule only the spin-allowed ESA transitions from state $^4T_2$ to states $^4A_2$ and $^4T_{1b}$ should be observed with a reasonable intensity. According to the results given in Tables VII and VIII the zero-phonon positions of these vibronic transitions should be located around 7300 $\rm cm^{-1}$ ($\cong$1370 nm) and 12 500 $\rm cm^{-1}$ ($\cong$800 nm); these positions agree well with the experimental data.

We could be tempted to assign the observed ESA bands at around 800 nm and 1250–1300 nm to the spin-allowed transitions $^4T_2\rightarrow{}^4T_{1b}$ and $^4T_2\rightarrow{}^4A_2$ solely. This seems to be correct in the case of the low-energy band since the corresponding electron-phonon coupling factor $S_{\rm int}$ is large and the SCC model would predict a broad band. The width of this band is also well explained using the strong-field approach since it is associated with a transition between states having different electron configurations, $t_2^4e_g^3$ for $^4T_2$ and $t_2^3e_g^4$ for $^4A_2$, thus different equilibrium configurations. The case of the high-energy band (states $^4T_2$ and $^4T_{1b}$ with the same electron configuration $t_2^4e_g^3$ is more questionable since the model and the strong-field approach predict a weak-coupling factor, thus a narrow line when a broad band is observed.

Two reasons can be given to elucidate this point; a strong Jahn-Teller (JT) effect in the $^4T_2$ and/or the $^4T_{1b}$ excited states as was used in the case of the $\rm V^{2+}$ and $\rm Cr^{3+}$ ions,[39–42] or a tunneling effect in the vibronic states of the adjacent levels $^4T_{1b}$, $^2T_{1a}$, and $^2T_{2a}$.

For example Sturge and Guggenheim[26] have introduced a JT energy $E_{\rm JT}=500$ $\rm cm^{-1}$ and a phonon frequency $\hbar\omega_3=300$ $\rm cm^{-1}$ to account for the reduced SO splitting of about 70 $\rm cm^{-1}$ of state $^4T_2$ in $\rm KMgF_3{:}Co^{2+}$ (dynamic JT or Ham effect[43]). The same kind of reduction is found in $\rm KZnF_3{:}Co^{2+}$ since we observe a splitting of about 80 $\rm cm^{-1}$ when theory predicts, for $\xi=535$ $\rm cm^{-1}$ a splitting of about 350 $\rm cm^{-1}$.

TABLE VII. Approximative ESA transition energies (zero-phonon positions) and energy shifts of potential curves relative to state $^4T_2$ in $\rm KZnF_3{:}Co^{2+}$.

Optical transitions		Energies	$S^i_{\rm int}\hbar\omega_0$
$^4T_2\rightarrow$	$^2E_a(\Gamma_8)$	5800	0
	$^4A_2(\Gamma_8)$	7250	695
	$^2T_{1a}(\Gamma_8)$	10 850	513
	(Γ_6)	11 450	
	$^2T_{2a}(\Gamma_8)$	11 525	485
	(Γ_7)	11 750	
	$^4T_{1b}(\Gamma_{8a})$	12 100	1
	(Γ_7)		
	(Γ_{8b})		
	(Γ_6)	13 150	
	$^2T_{1b}(\Gamma_6,\Gamma_8)$	14 750	450

TABLE VIII. Approximative ESA transition energies (zero-phonon positions) and energy shifts of potential curves relative to state $^4T_2$ in $\rm MgF_2{:}Co^{2+}$.

Optical transitions		Energies	$S^i_{\rm int}\hbar\omega_0$
$^4T_2\rightarrow$	$^2E_a(\Gamma_8)$	5625	0
	$^4A_2(\Gamma_8)$	7400	780
	$^2T_{1a}(\Gamma_8)$	10 870	603
	(Γ_6)	11 450	
	$^2T_{2a}(\Gamma_8)$	11 530	748
	(Γ_7)	11 750	
	$^4T_{1b}(\Gamma_{8a})$	12 200	5
	(Γ_7)		
	(Γ_{8b})		
	(Γ_6)	13 700	
	$^2T_{1b}(\Gamma_6,\Gamma_8)$	15 200	810

Following this argument, two types of $^4T_2\rightarrow{}^4T_{1b}$ ESA transitions would occur and for $E_{\rm JT}\cong500$ $\rm cm^{-1}$ they would be shifted to the high energies according to the expressions,[40]

$$E_1=\Delta E+E_{\rm JT}=\Delta E+500\ {\rm cm^{-1}}\ ,$$

$$E_2=\Delta E+4E_{\rm JT}=\Delta E+2000\ {\rm cm^{-1}}\ ,$$

where ΔE stands for the separation of the two states in the absence of the JT effect. In addition, the widths at half maximum and at high temperature of these bands would be given by[39–42]

$$\Delta_1=(16\ln2)^{1/2}(E_{\rm JT}kT)^{1/2}\cong1076\ {\rm cm^{-1}}\ ,$$

$$\Delta_2=(64\ln2)^{1/2}(E_{\rm JT}kT)^{1/2}\cong2153\ {\rm cm^{-1}}\ .$$

These widths would correctly describe the experimental data. However, we do not observe shifts as high as 500 and 2000 $\rm cm^{-1}$ since the positions of the ESA transitions, as predicted in the absence of the JT effect, are quite satisfactory.

It seems difficult to invoke the JT effect solely to account for the wide ESA band around 800 nm. On the contrary, if a strong tunneling effect occurs between the vibronic states of levels $^4T_{1b}$, $^2T_{1a}$, and $^2T_{2a}$, the spin selection rule is relaxed and the transitions to the doublet states borrow some intensity from the transition to the quartet state. This phenomenon has been invoked, for example, in gadolinium-scandium-gallium garnet $\rm GSGG{:}Cr^{3+}$ between the states ^2E and $^4T_2$ to account for the thermal behaviors of the fluorescence intensities and lifetimes in this material.[44–46]

Within this hypothesis the positions and the shapes of the observed ESA bands can be described very accurately. This is illustrated in Fig. 12 in the case of $\rm MgF_2{:}Co^{2+}$ by using the parameters of Table VIII for state $^2T_{2a}$ in the case of the band at around 800 nm and those for state $^4A_2$ for the band at around 1300 nm, that is $S_{\rm int}\hbar\omega_0=748$ and 780 $\rm cm^{-1}$, with $\hbar\omega_0=326$ $\rm cm^{-1}$, respectively. The fits are good for zero-phonon transition energies of about 11 700 and 7200 $\rm cm^{-1}$, which agree well with the approximate values reported in Table VIII. In the case of the band at around 800 nm (12 500 $\rm cm^{-1}$) the maximum of the $^4T_2\rightarrow{}^2T_{2a}$ ESA phonon sideband almost coincides

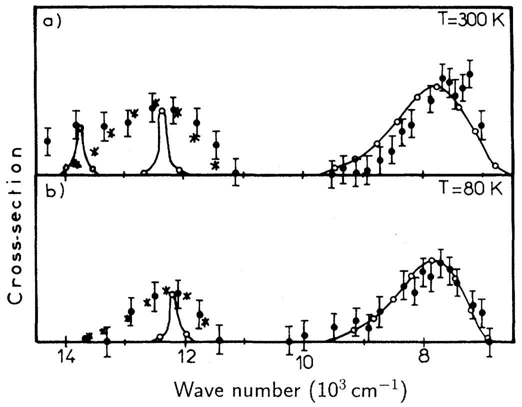

FIG. 12. Fitting of the σ polarized ESA band shape in MgF_2:Co^{2+} (●) at (a) $T=300$ K and (b) 80 K line-shape functions W_p associated with the spin-allowed transitions $^4T_2 \rightarrow {}^4A_2$ (for the band around 8000 cm^{-1}) and $^4T_2 \rightarrow {}^4T_{1b}$ (for the band around 12 500 cm^{-1}) (○) but also using the line-shape function (for the band around 12 500 cm^{-1}) associated with the $^4T_2 \rightarrow {}^2T_{2a}$ transition (∗).

with the position of the $^4T_2 \rightarrow {}^4T_{1b}$ ESA peak; this can also be seen in Fig. 9.

V. LASER OPERATION

Room-temperature laser operation was only reported in the past[14] in the case of MgF_2:Co^{2+}. We report now on room-temperature laser operation of both MgF_2:Co^{2+} and $KZnF_3$:Co^{2+} under pulsed laser excitation at 1.32 μm.

The arrangement of equipment for these laser-pumped laser experiments is shown in Fig. 13. The laser crystals were placed on a water-cooled copper finger and were positioned at Brewster's incidence at a center of a nearly confocal resonator formed by two 25 cm radius mirrors separated by a distance of about 26 cm. For such a symmetric laser resonator, the TEM_{00} fundamental mode radius ω_c is about 280 μm. The beam waist value is calculated using the equation[47]

$$\omega_c = \frac{\lambda}{2\pi}[L(2R-L)]^{1/2}, \tag{6}$$

where R is the radius of the mirrors, L their separation, and λ the laser wavelength.

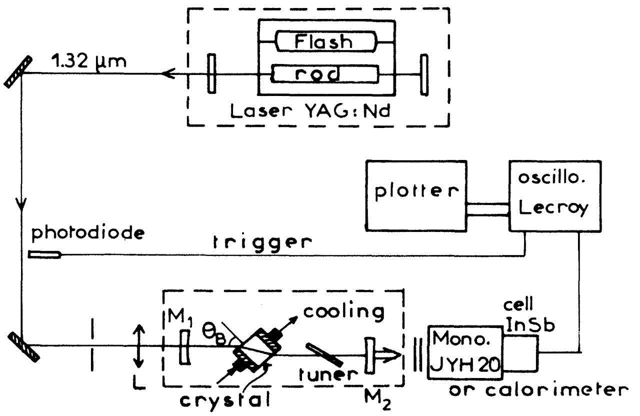

FIG. 13. Nd:YAG laser pumped cobalt laser: experimental arrangement.

The entrance mirror, labeled $M1$, is a dichroic mirror which had a high broad-band reflectivity (more than 99.5%) at the laser wavelength between about 1.9 and 2.1 μm and a high transmission (about 80%) at 1.32 μm. The output mirror labeled $M2$ is a mirror which transmits either 0.3% or 2.5% around 2 μm. Wavelength tuning was accomplished with a single quartz-crystal birefringent plate, 300 μm thick, placed at Brewster's angle.

Laser pumping was provided by a home-built flash-pumped Nd:YAG laser made of a 10 cm long and 7 mm diameter laser rod (from Crismatec in France) placed at the center of a 41 cm long flat-flat resonator which consisted of two plane mirrors, one being highly reflective and the other having a transmission of about 20% at 1.32 μm. The laser delivered 60 μs wide (at half maximum) laser pulses up to about 250 mJ. This unpolarized pump beam was focused onto the Co-doped laser crystals through the input mirror $M1$ with the aid of a lens of 15 cm focal length, which gave a pump beam waist ω_p of about 350 μm. This pump spot size was kept larger than the waist of the cavity to avoid damage to the crystals. Added to the fact that the pump beam was nonpolarized, these experimental conditions were far from being optimized and very modest laser performance was expected.

Figure 14 shows the slope efficiency curves obtained in the case of MgF_2:Co^{2+} without a birefringent tuning filter in the cavity. About 70% of the incident pump

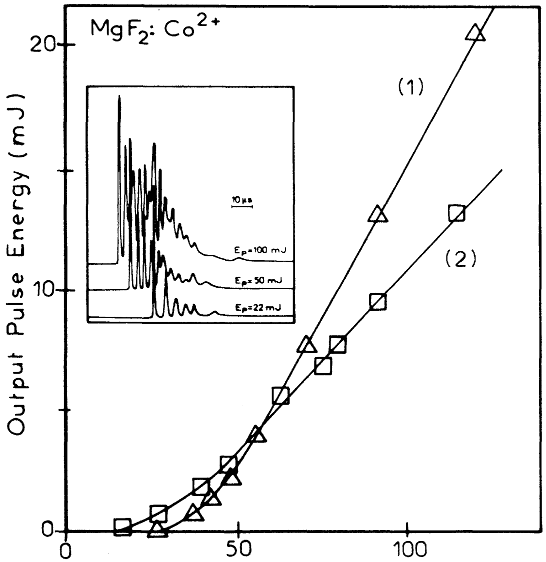

FIG. 14. Room-temperature laser slope efficiency curves in MgF_2:Co^{2+} for the two output coupler transmissions (1) $T=2.5\%$ and (2) $T=0.3\%$ and profile and evolution of the laser pulse with the incident pump energy (70% is absorbed by the crystal).

power was absorbed in the crystal and the free running laser wavelength was found at 2040 nm. More than 20 mJ were produced with a differential slope efficiency of about 25% with the 2.5% output coupler. Threshold-absorbed pump energies of about 15 and 27 mJ were obtained with the 0.3% and 2.5% output couplers, respectively. The figure also exhibits the profile of the laser pulse and its evolution with the pumping power; as already reported by Moulton,[13] the laser pulse presents characteristic relaxation oscillations (spikes), the time delay, and the number and intensity of the peaks which vary with the excitation pump power (variations which can be described by appropriate rate equations involving the optical losses through the photon lifetime in the cavity).

Figure 15 shows the laser tuning curve obtained with $MgF_2:Co^{2+}$, with the transmission curve of the output cavity mirror *M*2 which constitutes, with the birefringent filter (because of the order hops), the principal elements responsible for its wavelength limitation, from 1960 to 2180 nm.

In the case of $KZnF_3:Co^{2+}$ the laser performance was not so good. Figure 16 displays its laser slope efficiency curve with the profile and the evolution of the laser pulse with the pump power. The crystal absorbed about 50% of the incident power and the free-running laser wavelength was 2024 nm. The birefringent tuning plate introduced too much loss into the cavity to allow for wavelength tuning and threshold-absorbed pump energies of about 30 mJ were found with both output couplers. More than 3 mJ of output energy was measured with a differential slope efficiency above a threshold of about 8%. The crystal was not pumped harder because we were too close to its damage threshold (lower than that of $MgF_2:Co^{2+}$ in spite of a better crystal quality).

These results can be used now to estimate the effective laser emission cross section in each material and to compare these values with those found from the spectrodynamical data.

The effective laser emission cross section (LECS) σ_{eff} appears in the equation which relates the threshold-absorbed pump energy E_{th}^{abs} to the laser parameters[13]

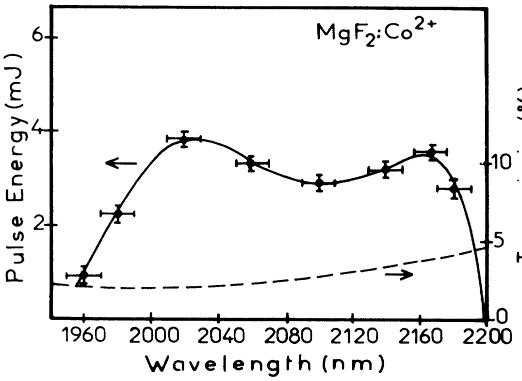

FIG. 15. Laser tuning curve recorded in $MgF_2:Co^{2+}$ (●) with the $T \cong 2.5\%$ output coupler and transmissions of this mirror (— — —).

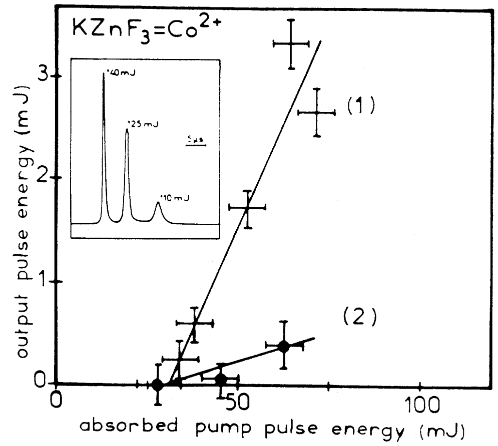

FIG. 16. Room-temperature laser slope efficiency curves in $KZnF_3:Co^{2+}$ for the two output coupler transmissions (1) $T=2.5\%$ and (2) $T=0.3\%$ and profile and evolution of the laser pulse with the incident pump energy (50% is absorbed in the crystal).

$$E_{th}^{abs}=\frac{h\pi c n(\omega_c^2+\omega_p^2)(L+T)}{4\sigma_{eff}\lambda_P\varepsilon}\,\frac{\tau_p}{\tau_f[1-\exp(-\tau_p/\tau_F)]}\,, \tag{7}$$

where τ_P and λ_P are the pump laser pulse width and wavelength, respectively, τ_F is the fluorescence lifetime at the operating temperature, and ε the pumping efficiency. L, the round-trip losses in the cavity other than that due to the transmission T of the output mirror, can be determined by using Eq. (7), knowing the laser thresholds E_1 and E_2 obtained for different output coupler transmissions T_1 and T_2, according to the equation

$$L=\frac{E_2T_1-E_1T_2}{E_1-E_2}\,. \tag{8}$$

This method can be used when the laser thresholds are known with good precision; this is the reason why only the case of $MgF_2:Co^{2+}$ will be considered in the following treatment.

In the case of ESA at the laser wavelength, the effective LECS σ_{eff} is related to the ESA cross section σ_{esa} (as found experimentally) by

$$\sigma_{eff}=\sigma_{em}-\sigma_{esa}\,, \tag{9}$$

where σ_{em} is the stimulated emission cross section which can be calculated from the emission spectrum $N(\lambda)$, given in photons per unit wavelength interval and per second, with the equation[48,49]

$$\sigma_{em}(\lambda)=\frac{\lambda^4}{8\pi c\tau_R n^2}\,\frac{N(\lambda)}{\int_0^\infty N(\lambda)d\lambda}\,, \tag{10}$$

where τ_R stands for the radiative lifetime and is related to the fluorescence lifetime by the fluorescence quantum efficiency $\eta=\tau_F/\tau_R$.

Since no excited-state absorption was found at the laser wavelength (see previous section), it is expected that $\sigma_{eff} \cong \sigma_{em}$.

The parameter values used to make the calculations in the case of $MgF_2:Co^{2+}$ were the following: $\omega_c \cong 280$ μm, $\omega_p \cong 359$ μm, $\lambda_p = 1.32$ μm, $\tau_P \cong 60$ μs; $\tau_R \cong 6$ ms; $\tau_F \cong 30$ μs; $n = 1.38$, $E_1 \cong 5$ mJ for $T_1 = 0.003$, and $E_2 \cong 27$ mJ for $T_2 = 0.025$.

It was found $L = 2.5-6\%$ and, at $\lambda = \lambda_{\text{laser}} = 2.04$ μm, $\sigma_{\text{eff}} \cong (2.1 \pm 0.4) \times 10^{-21}$ cm^2 for $\sigma_{\text{em}} \cong \frac{1}{3}(2\sigma^{\sigma}_{\text{em}} + \sigma^{\pi}_{\text{em}}) \cong 2.4 \times 10^{-21}$ cm^2, which is in good agreement and confirms that $\sigma_{\text{esa}} \cong 0$ in this emission domain.

Our effective LECS σ_{eff} also perfectly agrees with the value obtained in the past by Moulton.[13] At that time this author also compared this value with σ_{em} and found a great discrepancy that he tentatively explained by a low quantum efficiency. This hypothesis is now confirmed. Indeed Moulton estimated σ_{em} by assuming $\tau_R \cong 1.7$ ms, the fluorescence lifetime he measured at low temperature. It is clear that the true radiative lifetime is much longer (the absorption data discussed in Sec. III gave $\tau_R \cong 6$ ms) and that his σ_{em} value was overestimated.

VI. CONCLUSION

The spectroscopy and the fluorescence dynamics in the Co^{2+}-doped crystals $KZnF_3$, $KMgF_3$, MgF_2, and MgO have been studied in detail and the results compared with the predictions of the single-configuration-coordinate (SCC) model. The position and the shape of the main bands of the ground-state absorption (GSA) and emission spectra agree well with these predictions. It leads to the determination of all the energy levels of the Co^{2+} ion, and examination of the infrared fluorescence lifetime with temperature reveals the importance of the nonradiative relaxation processes and the extremely low fluorescence quantum efficiency in these materials.

The excited-state absorption (ESA) spectra of the Co^{2+}-doped $KZnF_3$ and MgF_2 single crystals have been recorded at low and at high temperatures. Two bands are found in the near-infrared domain with cross sections of the same order of magnitude as those of the GSA bands. ESA occurs in the pumping domain of these laser crystals around 1.32 μm, but it is negligible in the region of stimulated emission. The position and the shape of these bands are also compared with the predictions of the SCC model and the agreement seems satisfactory, assuming the possibility of ESA transitions towards vibronically coupled (tunneling effect) spin doublet and quartet states.

Room-temperature laser operation has been obtained, under the same conditions, in $KZnF_3:Co^{2+}$ as well as in $MgF_2:Co^{2+} \cdot MgF_2:Co^{2+}$ shows better thermomechanical properties and better laser performance and the results are used to ascertain the value of the radiative lifetime in this material and to confirm the absence of ESA in the stimulated emission domain.

ACKNOWLEDGMENTS

We wish to thank the colleagues designated in Sec. II for providing the different single crystals, A. Laggrifoul and B. Varrel for their technical assistance and B. M. Industries and Crismatec for providing the different elements of the flashlamp-pumped YAG:Nd laser used in this work. This work was performed under the auspices of the Centre National de la Recherche Scientifique (CNRS) and of the Direction des Recherches et des Etudes Techniques (DRET) in France. The Laboratoire de Physico-Chimie des Matériaux Luminescents is "Unité Associée No. 422 au CNRS."

---

[1] L. F. Johnson, H. J. Guggenheim, and R. A. Thomas, Phys. Rev. **149**, 157 (1966).

[2] L. F. Johnson, R. E. Dietz, and H. J. Guggenheim, Phys. Rev. Lett. **11**, 318 (1963).

[3] L. F. Johnson, R. E. Dietz, and H. J. Guggenheim, Appl. Phys. Lett. **5**, 21 (1964).

[4] P. F. Moulton, A. Mooradian, and T. B. Reed, Opt. Lett. **3**, 164 (1978).

[5] F. Auzel and R. Moncorgé, J. Opt. (Paris) **15**, 338 (1983).

[6] R. Moncorgé, F. Auzel, and J. J. Breteau, Philos. Mag. B **51**, 489 (1985).

[7] P. F. Moulton and A. Mooradian, Appl. Phys. Lett. **35**, 838 (1979).

[8] P. F. Moulton, IEEE J. Quantum Electron. **18**, 1185 (1982).

[9] W. Kunzel, W. Knierim, and V. Dürr, Opt. Commun. **36**, 383 (1981).

[10] K. R. German, V. Dürr, and W. Kunzel, Opt. Lett. **11**, 12 (1986).

[11] J. C. Walling, H. P. Jenssen, R. C. Morris, E. W. O'Dell, and O. G. Peterson, Opt. Lett. **4**, 182 (1979).

[12] J. C. Walling, O. G. Peterson, and R. C. Morris, IEEE J. Quantum Electron. **16**, 120 (1980).

[13] P. F. Moulton, IEEE J. Quantum Electron. **21**, 1582 (1985).

[14] D. Welford and P. F. Moulton, Opt. Lett. **13**, 975 (1988).

[15] C. Ridou, M. Rousseau, and F. Gervais, J. Phys. C **19**, 5757 (1986).

[16] H. Harmand, Ph.D. thesis, Université de Grenoble, 1985.

[17] R. Burriel, J. Bartolomé, D. Gonzales, R. Navarro, C. Ridou, M. Rousseau, and A. Bulou, J. Phys. C **20**, 2819 (1987).

[18] M. D. Sturge, Phys. Rev. B **8**, 6 (1973).

[19] R. Almairac, Ph.D thesis, Université de Montpellier, 1975.

[20] M. J. L. Sangster and C. W. McCombie, J. Phys. C **3**, 1498 (1970).

[21] W. Low, Phys. Rev. **109**, 256 (1958).

[22] A. D. Liehr, J. Phys. Chem. **67**, 1314 (1963).

[23] H. M. Gladney, Phys. Rev. **146**, 253 (1966).

[24] M. D. Sturge, Phys. Rev. **140**, 880 (1965).

[25] J. E. Ralph and M. G. Townsend, J. Chem. Phys. **48**, 149 (1968).

[26] M. D. Sturge and H. J. Guggenheim, Phys. Rev. B **4**, 2052 (1971).

[27] A. J. Mann and P. J. Stephens, Phys. Rev. B **9**, 863 (1974).

[28] S. Muramatsu and N. Sakamoto, J. Phys. Soc. Jpn. **46**, 1273 (1979).

[29] F. Auzel, J. M. Breteau, and R. Moncorgé (unpublished).

[30] L. T. Peixoto and M. E. Foglio, Phys. Rev. B **32**, 2596 (1985); **33**, 2842 (1986).

[31] J. M. Breteau, Ph.D thesis, Université de Paris, 1986.

[32] T. Benyattou, Ph.D thesis, Université de Lyon I, 1987.

[33] R. Moncorgé and T. Benyattou, Phys. Rev. B **37**, 9186 (1988), and references therein for the Ni^{2+}-doped systems.

[34] C. W. Struck and W. H. Fonger, J. Lumin. **10**, 1 (1975).

[35] K. Huang and A. Rhys, Proc. R. Soc. London, Ser. A **204**, 406 (1950).

[36] R. Moncorgé and T. Benyattou, Phys. Rev. B **37**, 9177 (1988).

[37] D. Curie, in *Optical Properties of Ions in Solids*, edited by B. Di Bartolo (Plenum, New York, 1975).

[38] D. F. Nelson and M. D. Sturge, Phys. Rev. A **137**, 1117 (1965).

[39] A. Payne, L. L. Chase, and G. D. Wilke, Phys. Rev. B **37**, 998 (1988).

[40] H. W. H. Lee, S. A. Payne, and L. L. Chase, Phys. Rev. B **39**, 8907 (1989).

[41] K. Petermann, Opt. Quantum Electron. **22**, 199 (1990).

[42] J. A. Caird, S. A. Payne, P. R. Staver, A. J. Ramponi, L. L. Chase, and W. F. Krupke, IEEE J. Quantum Electron. **25**, 1077 (1988).

[43] F. S. Ham, Phys. Rev. A **13**, 1727 (1964).

[44] C. J. Donnelly, T. J. Glynn, G. P. Morgan, and G. F. Imbush, J. Lumin. **48/49**, 283 (1991), and references therein.

[45] M. Yamaga, B. Henderson, K. P. O'Donnell, and C. Trager Cowan, Appl. Phys. B **50**, 425 (1990).

[46] M. Yamaga, B. Henderson, K. P. O'Donnell, and G. Yue, Appl. Phys. B **51**, 132 (1990).

[47] P. W. Milonni and J. H. Eberly, in *Lasers* (Wiley, New York, 1988).

[48] D. E. McCumber, Phys. Rev. A **134**, 299 (1964); **134**, 964 (1964).

[49] P. F. Moulton, J. Opt. Soc. Am. **3**, 125 (1986).